JOURNAL OF MAGNETIC RESONANCE **124,** 323–342 (1997)
ARTICLE NO. MN961025

A Comparison between Different Imaging Strategies for Diffusion Measurements with the Centric Phase-Encoded TurboFLASH Sequence

J. COREMANS,* M. SPANOGHE,* L. BUDINSKY,† J. STERCKX,*,‡ R. LUYPAERT,* H. EISENDRATH,§ AND M. OSTEAUX*

*Biomedical MR Unit, PRIMIS, Vrije Universiteit Brussel, Laarbeeklaan 101, 1090 Brussels, Belgium; †Institute of Measurement Science, SAS, Bratislava, Slovakia; ‡ELEC, Faculty of Applied Sciences, Vrije Universiteit Brussel, Pleinlaan 2, 1050 Brussels, Belgium; and §Magnetic Resonance, Department of Physics, Faculty of Sciences, Vrije Universiteit Brussel, Pleinlaan 2, 1050 Brussels, Belgium

Received April 22, 1996; revised October 3, 1996

The study compared the results of three centrally reordered phase-encoded turboFLASH sequences for diffusion-weighted imaging (DWI). The sequences were conventional turboFLASH, turboFLASH with subtraction of T_1-related effects, and turboFLASH with correction for T_1-related effects during the imaging period only. The relative merits were studied with respect to image quality and accuracy by computer simulation and by experimental validation on phantoms and on *in vivo* rat brain. A T_1-related underestimation of the diffusion coefficient ranging from −30% ($T_1 \approx 200$ ms) to −5% ($T_1 \approx 1$ s) was found to exist for the conventional sequence. Image artifacts, caused by longitudinal relaxation during the imaging period, are reflected in calculated diffusion maps. When the correction sequence is used, the artifacts and the systematic errors are reduced but longitudinal relaxation during the delay between preparation and imaging periods remains large enough to induce significant errors (−15% for $T_1 \approx 200$ ms to −3% for $T_1 \approx 1$ s). The subtraction sequence eliminates the influence of T_1 effects on the calibrations, but leads to identical artifacts for all diffusion-weighted images.

INTRODUCTION

In the detection of stroke lesions, diffusion-weighted imaging (*1*) (DWI) has proven to provide unique information about early pathological changes. Experimental (*2*) and clinical studies (*3*) of acute cerebral ischemia have shown that ischemic lesions may be detected in the early phase of the brain infarct due to a decrease of the so-called apparent diffusion coefficient (ADC). Several animal models were designed to elucidate questions concerning the detection and genesis of ischemic brain lesions. Among the issues addressed with these models, some relate to the detection accuracy of the lesion extent at an early stage (*4*), and others describe the relationship between the ADC parameter and the perfusion status (*5*) or investigate the existence of an ADC threshold below which lesions evolve irreversibly to an infarct (*6*).

Diffusion-weighted MRI techniques aimed at the determination of the ADC values that correspond to characteristic features in the evolution of the disease must fulfill specific requirements. Ideally, the measurements should be performed with an accuracy corresponding to the smallest changes in ADC which can be related to changes in the pathophysiology of the disease. Diffusion-weighted images must be acquired rapidly in order to produce motion-free diffusion-weighted images. Moreover, when the method is applied in the clinical environment, the total imaging time must be kept short since it takes up part of the ''therapeutic window.'' In experimental model conditions, most of the studies involving DWI are complemented by other techniques, and the entire set of measurements should occur on a time scale which is short with respect to the evolution of the lesion.

Among the imaging techniques available for these purpose, echo-planar imaging (*7*) is the technique of choice but places high demands on the hardware. Considering the restricted hardware capabilities existing at many sites, the usefulness of turboFLASH in this context was investigated. This technique combines typical imaging times of 300–1000 ms with a high spatial resolution capability. It consists of a preparation period which determines the desired contrast, followed by a short TR gradient-echo imaging period (*8*). For diffusion-weighted turboFLASH, the preparation period consists of a pair of diffusion-sensitizing gradient pulses which are incorporated into a driven-equilibrium Fourier transform (DEFT) scheme (*9*). Initial studies have demonstrated that DWI could be successfully achieved in this way on phantoms and healthy volunteers (*10–12*). These studies were performed on clinical imaging systems with typical maximum gradient amplitudes of $\pm 10\sqrt{3}$ mT/m and $\Delta =$ 50 ms, producing diffusion-weighting b factors up to 59,000 s/cm^2. However, detection of stroke lesions requires heavily diffusion-weighted images, with typical b values around 100,000 s/cm^2 (*2, 3*).

1090-7807/97 $25.00

Generally, for free diffusion characterized by a diffusion coefficient D, the diffusion coefficient is obtained by fitting the image intensities S_i of diffusion-weighted images i to the equation $A\exp(-b_i D)$, or by performing a linear regression of $\ln S_i$ versus b_i. The diffusion weighting is given by the factor b_i and is calculated by taking into account all gradients present in the sequence (*1*). Typically, the accuracy of the technique can be assessed by performing calibration measurements on liquids with known diffusion coefficient and extracting the diffusion coefficient from the slope of the semilogarithmic plot of S_i versus b_i. When the diffusion-weighted turboFLASH sequence is implemented with b values in the range of up to 100,000 s/cm^2, a systematic deviation of the linear relationship was found, implying a loss of accuracy (*13*). The deviation could be attributed to longitudinal relaxation effects during the preparation and the imaging period. Longitudinal relaxation during the acquisition of the image is also known to degrade the desired contrast when using a magnetization-prepared sequence (*14*). This was the case for diffusion-weighted images acquired with turboFLASH, where characteristic edge artifacts appeared in the phase-encoding direction due to the varying magnetization during the imaging period. Strategies aiming primarily to overcome these image artifacts have been described in the past for T_2-weighted (*15*) and diffusion-weighted turboFLASH sequences (*16*).

The purpose of this work was to determine whether these strategies could provide accurate diffusion data. Their relative merits were assessed with respect to accuracy and with respect to the image quality of diffusion-weighted images and associated calculated diffusion maps. This was realized by performing computer simulations, based on theoretical expressions for the different strategies, which were experimentally verified on phantoms. As an *in vivo* example, diffusion-weighted turboFLASH images and diffusion maps from rat brain were compared to similar images using the spin-echo imaging sequence which was taken as the ''gold standard.''

THEORETICAL CONSIDERATIONS

We wish to describe the evolution of the transverse magnetization during the acquisition of diffusion-weighted turboFLASH images. We consider a spoiled, slice-selective, FLASH sequence in which all transverse magnetization is eliminated at the end of each repetition cycle (perfect spoiling). The diffusion-weighted preparation consists of a pair of diffusion-sensitizing gradient pulses incorporated into a DEFT scheme (Fig. 1).

The first sequence (referred to as the conventional sequence) comprises a preparation period with an RF pulse train $[90^\circ_x\text{—}\mathrm{TE_p}/2\text{—}180^\circ_y\text{—}\mathrm{TE_p}/2\text{—}90^\circ_{-x}]_{\mathrm{prep}}\text{—}\tau\text{—}[\alpha_x]_n$, as described by Deimling *et al.* (*10*). The delay τ between the preparation period and the imaging period $[\alpha]_n$ is necessary to include large spoiling gradient pulses and to allow for the decay of possible residual eddy-current fields. The second sequence (referred to as the correction sequence) uses the same RF pulse train, but acquires two data sets, one of which, acquired by disabling the phase-encoding gradient, is used to correct the actual imaging data set (*16*). The third sequence [referred to as the subtraction sequence (*15*)] has $[90^\circ_x\text{—}\mathrm{TE_p}/2\text{—}180^\circ_y\text{—}\mathrm{TE_p}/2\text{—}90^\circ_{-x,x}]_{\mathrm{prep}}\text{—}\tau\text{—}[\alpha_{x,-x}]_n$ as preparation, where the last DEFT pulse and the slice-selective RF pulse are cycled in a two-phase cycling scheme while the receiver phase remains constant. In deriving the corresponding theoretical expressions, the following assumptions are made: ideal RF pulses, perfect spoiling during the delay τ and within the FLASH imaging part, and full relaxation between two consecutive experiments.

Conventional Sequence

The approach to steady state of the longitudinal magnetization for a spoiled FLASH sequence can be calculated by making use of the relationship between the longitudinal magnetization before and after the nth α pulse, together with the expression for the longitudinal relaxation during the time TR between two consecutive RF pulses (*17*). The longitudinal magnetization directly after the nth α pulse, $M_z(n, +)$ is given by

$$M_z(n, +) = M_z(n, -)\cos(\alpha), \qquad [1]$$

with $M_z(n, -)$ as the longitudinal magnetization immediately before the RF pulse. Between consecutive RF pulses, the longitudinal magnetization evolves by longitudinal relaxation as

$$M_z(n+1, -) = M_z(n, +)e^{-\mathrm{TR}/T_1} + M_0(1 - e^{-\mathrm{TR}/T_1}). \qquad [2]$$

After substituting Eq. [1] in Eq. [2] and expressing the result as a function of the magnetization for the first step, one obtains

$$M_z(n, -) = M_z(1, -)[E_1\cos(\alpha)]^{n-1} + M_0(1 - E_1)\frac{\{1 - [E_1\cos(\alpha)]^{n-1}\}}{[1 - E_1\cos(\alpha)]}, \qquad [3]$$

where M_0 stands for the equilibrium magnetization, α is the flip angle, $E_1 = \exp(-\mathrm{TR}/T_1)$, TR is the cycling time of the FLASH sequence, T_1 is the longitudinal relaxation time, and $M_z(1, -)$ is the longitudinal magnetization before the first α pulse. The magnetization $M_z(1, -)$ is determined by

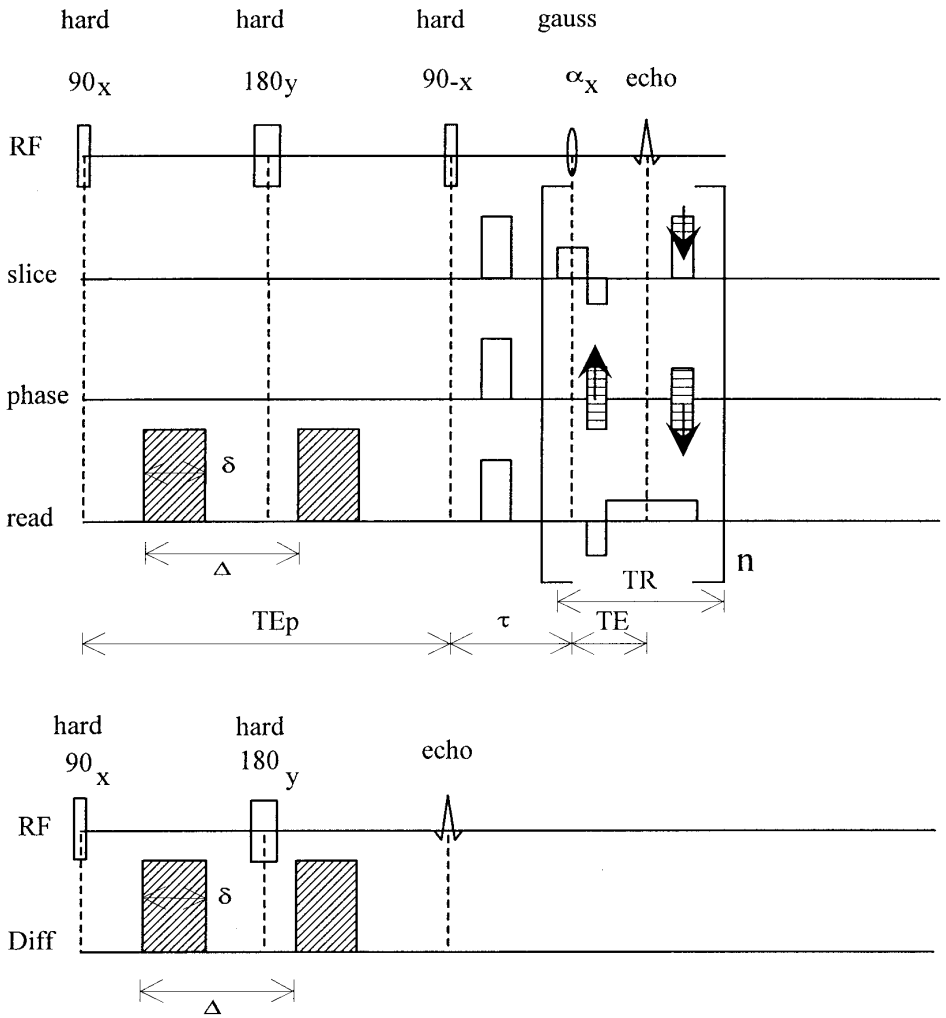

FIG. 1. Top: Diffusion-weighted turboFLASH sequence. A diffusion-weighted preparation period consists of a 90°—$TE_p/2$—180°—$TE_p/2$—90° RF pulse scheme, incorporating two diffusion-sensitizing gradient pulses with duration δ. The time between the onset of the gradient pulses is Δ. Gradient pulses during the delay τ are needed to spoil residual transverse magnetization. A gradient-spoiled FLASH imaging cycle with repetition time TR = 6.513 ms and echo time TE = 2.5 ms is repeated 64 times by using a centric phase-encoding scheme (0, ±1, ±2, . . .). Bottom: Stejskal–Tanner sequence for spectroscopic diffusion measurements. The timing was taken to be identical to the preparation period of the turboFLASH sequence.

the diffusion-weighted preparation period and the longitudinal relaxation during the delay τ:

$$M_z(1, -) = M_0E_2e^{-bD}e^{-\tau/T_1} + M_0(1 - e^{-\tau/T_1}), \quad [4]$$

where E_2 stands for $\exp(-TE_p/T_2)$ with TE_p as the preparation time, T_2 is the transverse relaxation time, D is the diffusion coefficient, and b is the gradient factor for the diffusion gradient pulses in the preparation period.

The transverse magnetization $M_t(n)$ after the nth α pulse, at $t = TE$, is given by

$$M_t(n) = M_z(n, -)e^{-TE/T_2^*}e^{-b_0D}\sin(\alpha), \quad [5]$$

where TE is the echo time of the FLASH sequence, b_0 is the b factor corresponding to the imaging part of the sequence, and T_2^* is the effective transverse relaxation time including possible inhomogeneity effects of the main magnetic field. In the remaining analysis, we have neglected the factor due to T_2^* since it is common to each excitation step n and to each diffusion-weighted experiment. The contribution b_0, evaluated as 10 s/cm^2 on the basis of the timing and amplitudes of the imaging gradient pulses for the zero phase-encoding step, has also been neglected.

Substitution of Eqs. [3] and [4] into [5] gives

$$M_t(n) = A(n)e^{-bD} + B(n) \quad [6]$$

with

$$A(n) = M_0 E_2 e^{-\tau/T_1}[E_1\cos(\alpha)]^{n-1}\sin(\alpha) \quad [7]$$

$$B(n) = \Big[M_0(1 - e^{-\tau/T_1}) \times [E_1\cos(\alpha)]^{n-1} + M_0(1 - E_1) \times \frac{\{1 - [E_1\cos(\alpha)]^{n-1}\}}{[1 - E_1\cos(\alpha)]} \Big]\sin(\alpha). \quad [8]$$

Equation [6] describes the evolution of the signal toward steady state and implies that subsequent phase-encoding steps are weighted differently, thereby imposing a filter along the phase-encoding direction in k space. The shape of the filter is determined by tissue parameters, e.g., T_1, and by instrumental parameter settings (e.g., TR, flip angle, phase-encoding order). After Fourier transformation, image artifacts will appear in the phase-encoding direction due to the filtering.

As mentioned previously, quantitative diffusion results are obtained by using a nonlinear fit of diffusion-weighted data $S(b)$ to the expression $A\exp(-bD)$ or by using a linear fit of the logarithm of the data $S(b)$, i.e., $\ln S(b)$ to b (*1*). Equation [6] shows that the transverse magnetization can be separated into a diffusion-dependent term $A(n)\exp(-bD)$ and a diffusion-independent term $B(n)$ originating from the longitudinal relaxation during the delay τ and during the time TR of each cycle. The presence of the diffusion-independent term implies that extracting the diffusion coefficient D from a fit of $\ln S(b)$ against b becomes impossible. As will be shown in the following sections, fitting of the data to the expression $A\exp(-bD) + B$ seemed to be more appropriate for this case.

Correction for the k-Space Filter Effects

Here, two sets of data are acquired: a first set $M'_t(n)$ of diffusion-weighted measurements is acquired without phase-encoding gradients and a second set consists of the actual image data $M_{t,\mathrm{im}}(n)$. The first set determines the evolution of the transverse magnetization $M'_t(n)$ as expressed by Eq. [6] and, when normalized to the value of the first excitation step, defines a function $w(n)$:

$$w(n) = \frac{M'_t(n)}{M'_t(n=1)}. \quad [9]$$

In practice, the function $w(n)$ was calculated by taking the peak values of the absolute value of the echo signal corresponding to $M'_t(n)$ and M'_t $(n = 1)$. The function serves to correct subsequently acquired image data $M_{t,\mathrm{im}}(n)$:

$$M_{t,\mathrm{corr}}(n) = M_{t,\mathrm{im}}(n)/w(n). \quad [10]$$

Disregarding the phase-encoding process for the moment, we can state that the filter governing the course of $M_{t,\mathrm{im}}(n)$ is in essence identical to $M'_t(n)$, and we obtain

$$M_{t,\mathrm{corr}}(n) = M'_t(n=1). \quad [11]$$

The corrected transverse magnetization remains constant through all the excitation steps of the imaging period and is given by

$$M_{t,\mathrm{corr}}(n) = [M_0 E_2 e^{-\tau/T_1} e^{-bD} + M_0(1 - e^{-\tau/T_1})]\sin(\alpha). \quad [12]$$

Again, Eq. [12] can be split into a diffusion-dependent and diffusion-independent term

$$M_{t,\mathrm{corr}}(n) = E(n)e^{-bD} + F(n) \quad [13]$$

with $E(n) = M_0 E_2 e^{-\tau/T_1} e^{-bD}\sin(\alpha)$ and $F(n) = M_0(1 - e^{-\tau/T_1})\sin(\alpha)$. Therefore, the same remark can be made here concerning the determination of the diffusion coefficient D by using the expression $\ln S(b)$ as a function of b for fitting the data.

Subtraction Sequence

With the subtraction sequence, the phases of the last 90° RF preparation pulse and of the slice-selective α RF pulse are changed according to $[90^\circ_x$—$\mathrm{TE_p}/2$—180°_y—$\mathrm{TE_p}/2$—$90^\circ_{(-x,x)}]_{\mathrm{prep}}$—$\tau$—$[\alpha_{(x,-x)}]_n$, while the receiver phase remains constant (x). The result is that the diffusion-independent term is eliminated from Eq. [6] and the transverse magnetization after the nth α pulse is given by

$$M_t(n) = 2M_0 E_2 e^{-\tau/T_1} e^{-bD}[E_1\cos(\alpha)]^{n-1}\sin(\alpha) \quad [14]$$

and thus

$$M_t(n) = 2A(n)e^{-bD}, \quad [15]$$

where $A(n)$ is described by Eq. [7]. Equation [15] shows that the diffusion coefficient can presently be derived by fitting the data to $\ln S(b)$ expressed as a function of b.

MATERIALS AND METHODS

Pulse Sequences

The RF pulse train in the preparation period consisted of hard pulses with a typical pulse width of 22 μs for a 90° pulse. Trapezoidal gradient diffusion-weighting pulses with a variable amplitude G were applied before and after the 180° RF pulse, yielding b factors from 0 to 94,727 s/cm^2

(Fig. 1). The b factors were calculated analytically according to the Stejskal–Tanner formula, including rise and fall times of the gradient pulses (*18*),

$$b = (\gamma G)^2[(\Delta - \delta/3)\delta^2 + \epsilon^3/30 - \epsilon^2\delta/6], \quad [16]$$

where γ is the gyromagnetic ratio for protons, G is the gradient strength, δ is the pulse duration, Δ is the duration between the start times of the two gradient pulses, and ϵ is the rise and fall time of the gradient pulses. In our case, ϵ is determined by the slew rate multiplied by the gradient strength. A delay τ of 4.882 ms was used between the preparation period and the imaging period. The imaging period consisted of a spoiled FLASH sequence (TR/TE = 6.513/2.5 ms) which included a variable (decreasing) spoiling gradient along the slice-select direction (*19*) and a rewinder in the phase-encoding direction. The combination of spoiler and rewinder gradients has been shown to rotate typical banding artifacts, caused by residual transverse coherences, parallel to the imaging plane (*20*). The amplitudes of the spoiler gradient were chosen experimentally to suppress the artifacts (decreasing amplitudes from 8 G/cm in 64 steps of 0.1 G/cm). To assess the efficiency of spoiling, the imaging sequence was adapted to provide a measurement immediately after the spoiling and rewinder gradients.

Slice selection was performed with a Gaussian-shaped RF pulse with a nominal flip angle of 7° or 20° and a duration of 512 μs (spectral width of 5.4 kHz, FWHM), which resulted in a slice thickness of 4.1 mm (phantom) and 2.2 mm (rat brain). The centric phase-encoding scheme (0, ±1, ±2, . . .) with 64 phase-encoding steps was chosen for all experiments. No data averaging was used (NEX = 1) except for *in vivo* imaging where NEX = 8 was used.

Simulations

To assess the effect of the *k*-space filter on the image quality and on the accuracy of the estimation of the diffusion coefficient, the image profile of a rectangular one-dimensional object was calculated for different parameter settings corresponding to the experimental results. The object had a width of 1.5 cm and was centered in the middle of the FOV. The Fourier transform $s(f_y)$ of the object was multiplied by a weighting function which corresponded to one of the courses of $M_t(n)$ described by Eq. [6], [12], or [14],

$$s'(f_y) = s(f_y)M_t(n) \quad [17]$$

with

$$s(f_y) = \int_{-\infty}^{\infty} \rho(y)e^{i2\pi f_y y}dy,$$

where $f_y = (\gamma/2\pi)G_yT$, with γ the gyromagnetic ratio for protons, G_y the phase-encoding gradient amplitude, T the phase-encoding gradient duration, and $\rho(y)$ the spin density.

The image of the object was then calculated by the inverse discrete Fourier transform of the sampled function $s'(f_y)$:

$$I(y_j) = \sum_{p=-N/2+1}^{N/2} s(p\Delta f_y)M_t(n)e^{-i2\pi p\Delta f_y y_j}\Delta f_y. \quad [18]$$

The relationship between the spacing and spatial frequency is given by $\Delta f_y = 1/N\Delta y = 1/\mathrm{FOV}$, where N is the number of samples in the y direction, Δy is the pixel width, and FOV is the field of view in the phase-encoding direction.

In Eq. [18], n stands for the excitation index within the FLASH sequence and determines the weighting of the phase-encoding step corresponding to the index p. A transformation $p = T(n)$ is necessary to link both indices so that Eq. [18] can be written as

$$I(y_j) = \sum_{n=1}^{N} s[T(n)\Delta f_y]M_t(n)e^{-i2\pi T(n)\Delta f_y y_j}\Delta f_y, \quad j = 1, 2, \ldots, N. \quad [19]$$

For a sequential phase-encoding scheme ($-N/2 + 1, \ldots, N/2$), the transformation is given by $T(n) = (n - N/2)$, while for a centric phase-encoding scheme (0, ±1, ±2, . . .), the transformation may be written as

$$T(n) = \frac{[1 - (-1)^{n-1}]}{4}\, n - \frac{(1 + (-1)^{n-1})}{4}\,(n - 1), \quad n = 1, 2, \ldots, N. \quad [20]$$

Image profiles $I(y_j)$ were calculated for several diffusion weightings and for parameter settings in accordance with the experimental results. The parameters involve the sequence parameters $\mathrm{TE_p}$, b, τ, TR, TE, α, matrix, and FOV used for the experiments, and the phantom-specific parameters T_1, T_2, and D. The values for the diffusion coefficient D were taken from the set of spectroscopic reference measurements for each sample. A value $M_0 = 1$ was taken for the entire set of simulations. The parameters were fed into expression [6], [12], or [14] for $M_t(n)$ and the image profiles were calculated. A region of interest was chosen in the central part of the image profile and the mean intensity was calculated. Diffusion coefficients were obtained by a nonlinear-least-squares analysis (SigmaPlot, Jandel Scientific, Erkrath, Germany) of the simulated data to monoexponential models

$$S = S_0e^{-bD} \quad [21]$$

and

$$S = S_0 e^{-bD} + B, \quad [22]$$

where S and S_0 represent the magnitude of the mean intensities with and without diffusion weighting, respectively, and B is taken constant. The b factor was calculated according to Eq. [16]. The diffusion coefficients obtained in this way were then compared to the input values of the simulation.

In order to account for possible slice effects, the course of the transverse magnetization $M_t(n)$, starting from the diffusion-modulated initial longitudinal magnetization $M_z(1, -)$, was calculated by solving the Bloch equations numerically for each phase-encoding step during the imaging period. The simulation was performed for slice-selective gradient pulses and Gaussian-shaped RF pulses that were matched in amplitude and duration to those used in the experiments. Between two subsequent RF pulses, perfect spoiling of transverse magnetization was assumed after each sampling period. Slice profiles were calculated with a resolution of 0.5 mm for each excitation step and the integral under the profile yielded the desired transverse magnetization $M_t(n)$. Image profiles of the one-dimensional object were again calculated and diffusion coefficients were obtained using the same procedure as stated previously.

Experimental Protocol

The experiments were performed on a 4.7 T system (SISCO, Palo Alto, California) with a bore diameter of 330 mm. The system is equipped with insert gradient coils with an internal diameter of 12.5 cm and providing maximum gradient strengths of ±100 mT/m in 250 μs.

Phantoms

The phantom material was made from a saline solution and agar–agar (3 wt%, Aldrich-Chemie, Belgium) doped with CuSO4 (Aldrich-Chemie). The agar solution was contained in plastic cylindrical tubes (14 mm i.d., 95 mm length) and sealed with parafilm. Agar was used to reduce convective flow within the tubes and to bring down the T_2 values into the range of brain tissue (*21*). The samples were placed individually in the middle of a homebuilt low-pass RF birdcage coil (4.5 cm i.d.), parallel to the main magnetic field. Temperature inside the magnet bore was monitored by means of a mercury thermometer (±0.2°C). The relaxation times T_1 and T_2 were determined spectroscopically using the inversion-recovery spin-echo sequence and the Carr–Purcell–Meiboom–Gill multiple-echo sequence, respectively. The peak amplitudes of the spectra were measured and analyzed using a nonlinear-least-squares method (Table 1).

Diffusion-weighted images of each sample with imaging parameters $\alpha = 7°$ or 20°, $\delta = 10$ ms, $\Delta = 25$ ms, $TE_p = 50$ ms, 128 × 64 matrix, 4.5 × 4.5 cm^2 FOV, NEX = 1, and 4.1 mm slice thickness were obtained for each of the three sequences. Regions of interest (ROI) were chosen in the center of the diffusion-weighted images of the samples. Each imaging experiment for a particular sequence and flip angle consisted of seven diffusion-weighting steps and was repeated a number of times. The imaging experiment was preceded and followed by a series of spectroscopic diffusion experiments in order to obtain a reference value of the diffusion coefficient and to observe possible temperature-dependent variations. A simple Stejskal–Tanner sequence (Fig. 1) with parameter settings identical to those imaging preparation was used for these measurements. Diffusion-weighted spectra were acquired from the entire sample and the absolute value of their peak amplitudes was determined. The data from the spectroscopic measurements and from the ROI were transferred to a PC and diffusion coefficients were calculated from a nonlinear-least-squares fitting the data to Eqs. [21] and [22], using the same software package as for the simulations.

TABLE 1
Relaxation Times of the Samples

	Concentration CuSO4 (g/liter)	T_1 (ms)	T_2 (ms)
Gel A	1.125	217 ± 1	36 ± 1
Gel B	0.495	463 ± 2	41 ± 1
Gel C	0.290	765 ± 3	46 ± 1
Gel D	0.170	1102 ± 4	47 ± 1

Note. Relaxation times (means ± SD, $n = 3$) obtained with inversion-recovery (IR) and Carr–Purcell–Meiboom–Gill (CPMG) Sequences for T_1 and T_2, respectively.

In Vivo

In vivo experiments were performed to compare the normal appearance of the brain as imaged with the navigator-corrected spin-echo sequence (*22*) to that obtained using the turboFLASH sequence. The experiments were performed on healthy female Wistar rats weighing 250–300 g. The rats were anesthetized with an intramuscular injection of a mixture (7/1) of ketamine hydrochloride (35 mg/kg, Ketalar, Parker Davis, Morris Plains, New Jersey) and Xylazine (5 mg/kg, Rompun, Bayer, Leverkusen, Germany). During the measurements, anesthesia was maintained by subcutaneous injection, using an infusion set at a fraction of $\frac{1}{3}$ of the above-mentioned mixture every 30 min. The head of the animal was positioned in a stereotaxic apparatus (flat skull position) mounted in the birdcage RF coil. Flexible carbon fiber electrodes were attached to the fore- and hindlimbs of the animal

for monitoring the ECG (Bruker, Physiogard SM785 NMR, Medizintechnik, Karlsruhe, Germany). All imaging experiments were triggered to the ECG of the animal. The ECG triggering resulted in repetition times of 6 to 12 s, yielding full relaxation for the brain tissue. The turboFLASH experiments were preceded by a diffusion-weighted navigator spin-echo imaging experiment (ECG triggered, TE = 48 ms, δ = 13.5 ms, Δ = 26 ms, 128 × 64 matrix, 3 × 4.5 cm^2 FOV, NEX = 1, slice = 2.2 mm). Sequence parameters for turboFLASH imaging were TE_p = 37 ms, δ = 13.5 ms, Δ = 17.5 ms, 128 × 64 matrix, 3 × 4.5 cm^2 FOV, NEX = 8, and slice = 2.2 mm. The smaller preparation time and averaging over eight acquisitions were necessary to obtain reasonable signal-to-noise ratios for the slice thickness of 2 mm. A slice thickness of 4.1 mm (as for the phantom study) resulted in partial volume effects which hindered the identification of structures within the brain.

Diffusion Maps

Diffusion maps of phantoms and ADC maps of rat brains were calculated from a series of diffusion-weighted images by performing a nonlinear-least-squares fit on a pixel-by-pixel basis. The diffusion-weighted images had a signal-to-noise ratio (SNR) large enough to avoid offsets due to the background noise (SNR $\geqslant$ 6) (*23*). The calculation program running on a SPARC-2 station (Sun Microsystems Inc., California) was derived from existing software (*24*), adapted for the SISCO data file format. The program was checked by calculating diffusion maps from several artificial diffusion-weighted images and comparing the statistical results with results obtained by commercial software (SigmaPlot, Jandel Scientific, Erkrath, Germany). The *b* factors for the navigator spin-echo images were calculated numerically. The calculation included rise and fall times of the gradient pulses and the presence of cross terms. A negligible deviation of 0.01% existed between analytic and numeric calculations of the *b* factor in a range of 0 to 200,000 s/cm^2 for the simple case of the spectroscopic Stejskal–Tanner diffusion sequence (Eq. [16]).

RESULTS AND DISCUSSION

Approach to Steady State

Examples of the T_1-dependent transient course of the signal during the imaging period are shown in Fig. 2. The data points represent measured signal curves for the sample with the largest T_1 and a nominal flip angle α of 20°. They are obtained by determining the absolute value of the echo amplitudes acquired without phase encoding. The signal curves were normalized to the first data point, thereby eliminating the influence of diffusion preparation. As such they represent the function $w(n)$ which describes *k*-space filter effects. The lines correspond to simulated data which represent the integrated signal intensity under the calculated slice profile for each excitation step. Including slice-profile effects (saturation of the central part with respect to the borders of the slice) is necessary to reproduce the general features of the signal curves. For example, the signal curve b_2 belonging to the conventional sequence has a slight minimum (5%) around excitation step n = 20, which could not be replicated on the basis of Eq. [6].

Although the major features of the signal curves are reproduced by the simulations, Fig. 2 (top and middle) shows that a discrepancy occurs between the measured and simulated signal curves. Since the signal curves are sensitive to the flip-angle distribution within the slice profile, the most probable source of error was expected to be found in matching experimental and simulated flip angles. Flip-angle calibration was performed nonselectively on the entire sample and flip-angle values were obtained by determining the transmission power value for which the signal ratio $S_\alpha/S_{90°} = \sin(\alpha)$, where $S_{90°}$ corresponded to the maximum measured signal. Using this transmission power in a slice-selective pulse calibration revealed a 15% change in flip-angle value. Discrepancies could also have been caused by the noise contribution on the first data point by which the signal curves were normalized, or by a mismatch between experimental and simulated diffusion weighting. The first contribution is more likely to occur for lower signal values, hence for higher *b* values. While this corroborates the results for the conventional sequence, it is not the case for the subtraction sequence where the experimental signal curves do overlap for all *b* values. A major mismatch in diffusion weighting would have been reflected in a difference between experimental and simulated attenuation plots (see next section), since the main signal is recorded during the first excitation steps for centric phase-encoded sequences.

Figure 2 (top) shows that for the conventional sequence, the course of the curves may increase or decrease depending on the choice of the *b* factor. The consequence for the centric phase-encoding scheme is that the filter will have a high-pass or low-pass characteristic, respectively. Each diffusion-weighted image will therefore exhibit a different edge artifact, which will be propagated into the calculated diffusion map. The figure shows that a high-pass filter will become more likely for increasing diffusion weightings. In general, the filter effect will be determined by the relative amplitude of the magnetization after the first excitation step with respect to its steady-state value. For instance, for the conventional sequence, the relative amplitudes are governed by multiple parameters describing the diffusion-preparation period (TE_p, T_2, b, D, τ, T_1) and the imaging period (α, T_1, TR).

The results for the subtraction and the correction sequence are shown in Fig. 2, middle and bottom, respectively. The

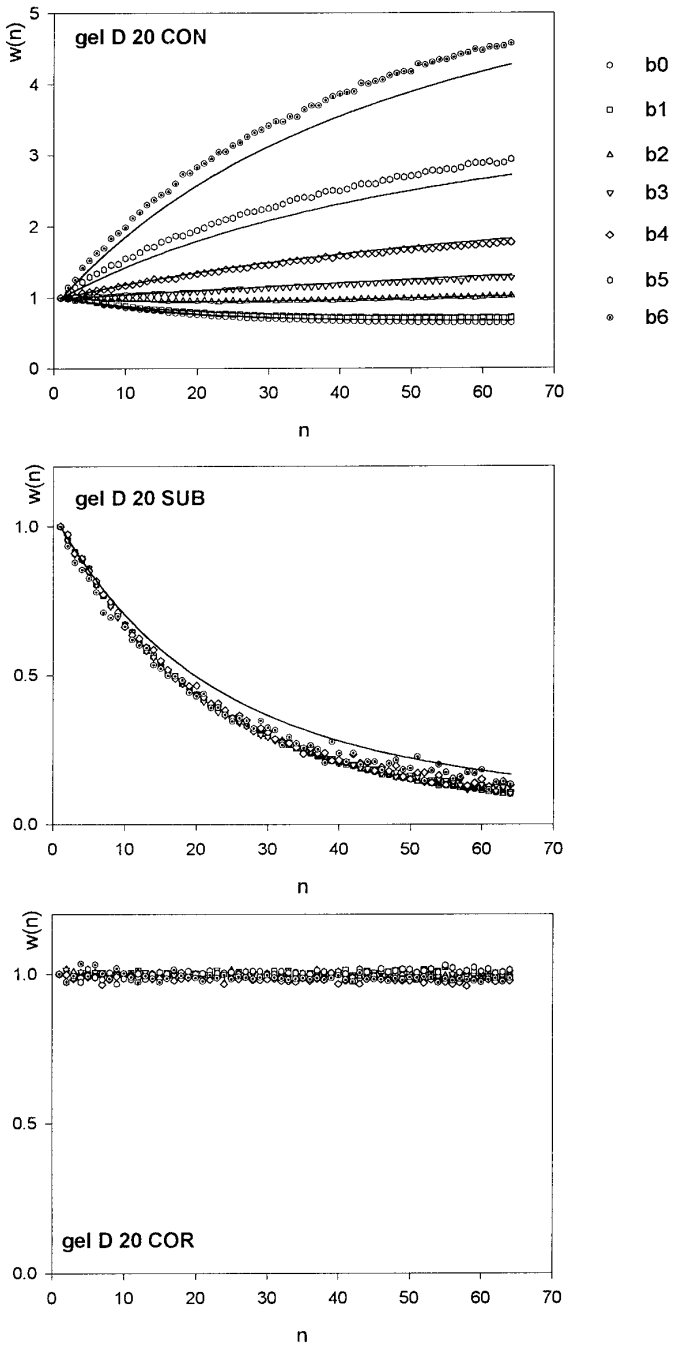

FIG. 2. Approach of transverse magnetization toward steady state during the imaging sequence (points, experimental; lines, simulations). The curves are normalized to the first data point and are presented for the sample with the largest T_1 (gel D), $\alpha = 20°$, and for several values of the b factor (in s/cm^2): $b_0 = 10$, $b_1 = 5931$, $b_2 = 23{,}683$, $b_3 = 37{,}013$, $b_4 = 53{,}294$, $b_5 = 72{,}537$, $b_6 = 94{,}737$. Top: The signal curves for the conventional sequence take different time courses which depend on the b factor used. A descending signal curve for small b factors changes gradually to a rising curve for larger b factors. Signal curves for other samples show different time courses depending on the specific relaxation times and sequence parameter values. Middle: The signal curves for the subtraction sequence decrease with n and coincide, irrespective of the range of the b factors used. The curves for the other samples show the same descending feature, which is governed by the parameters TR, T_1, and α. Bottom: Signal curves for the correction sequence. The signal curves have been corrected in order to present a flat time course. The time course is the same for the other samples as well. Simulations were not performed for this case.

striking difference with Fig. 2 (top) is that the signal intensity curves coincide for all values of the b factor. The curves in Fig. 2 (bottom) remain constant with increasing excitation step while a decrease is noticed for the curves in Fig. 2 (middle). These features are generally valid for the other samples as well. In contrast to the correction sequence, where no edge artifact is expected for flat signal curves, the subtraction sequence will suppress the high-frequency content of the images and produce blurring artifacts which will be identical for each diffusion-weighted image. As a result, the diffusion map will be widened in the phase-encoding direction with a severity corresponding to the blurring in the diffusion-weighted images.

Measurements of the residual transverse magnetization are shown in Fig. 3. The effectiveness of spoiling is demonstrated by a comparison of the signal measured with and without spoiling. The measurements were performed without diffusion weighting (largest signal) and for flip angles of 7°, 20°, 30°, and 90°. The residual signal is observed as intense lines parallel to the read-out direction. Each line corresponds to a separate MR signal having different phase encoding. The results show that no observable residual signal was detected for the flip angles used in this work. Furthermore, enhancement of the residual signal (as in GRASS) would have induced an oscillatory approach of the signal curves to steady state (*25*).

Simulated Image Profiles and Experiments

The effect of the k-space filter on the image quality has been assessed by calculating the image profiles of a one-dimensional object and are presented in Fig. 4. The normalized signal curves $w(n)$ were used to calculate the image profiles in order to show the filter effects and to allow comparisons with the original object. For gel A, the image profiles demonstrate edge-enhancement artifacts for both flip angles, which for the highest b values reach a magnitude of four times the average intensity of the central part of the image. The profiles for gel D vary from a loss of edge definition (low b) to edge enhancement (high b), depending on the choice of the flip angle and b value. These features are in contrast with the results for the subtraction sequence where the edges of the object are smoothed in all cases. The image profiles for the two b values coincide and the smoothing effect is more pronounced for larger flip angles.

Examples of the corresponding experimental diffusion-weighted images are shown in Fig. 5. In Fig. 5a, diffusion-

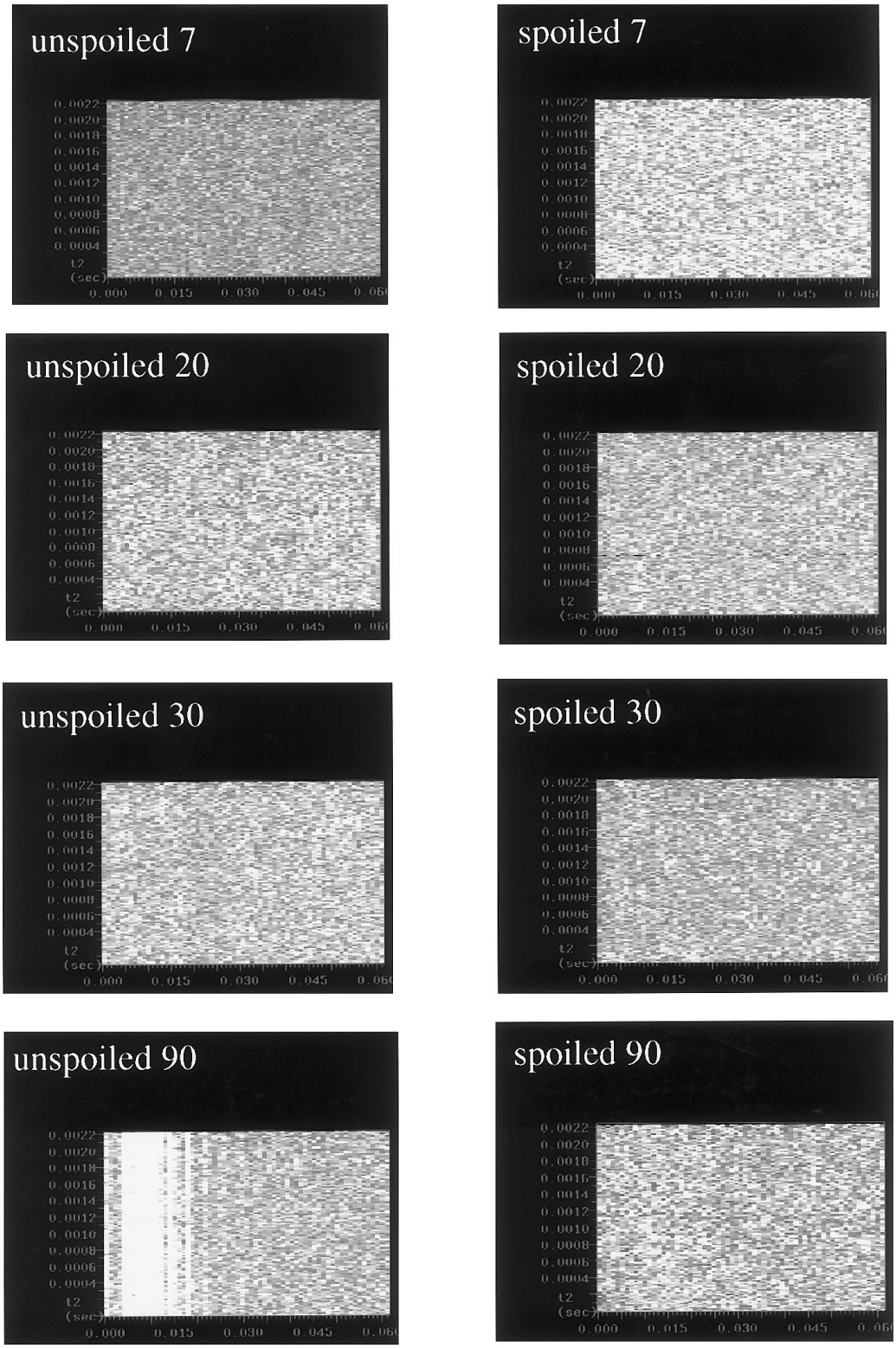

FIG. 3. Raw data acquired immediately after the spoiler and rewinder gradients in the imaging sequence: acquisition without (left column) and with (right column) spoiler gradient. Data were acquired from gel D with $b = 10$ s/cm^2 and $\alpha = 7°$, 20°, 30°, and 90°. Each vertical line in the data sets corresponds to the measurement of the transverse magnetization.

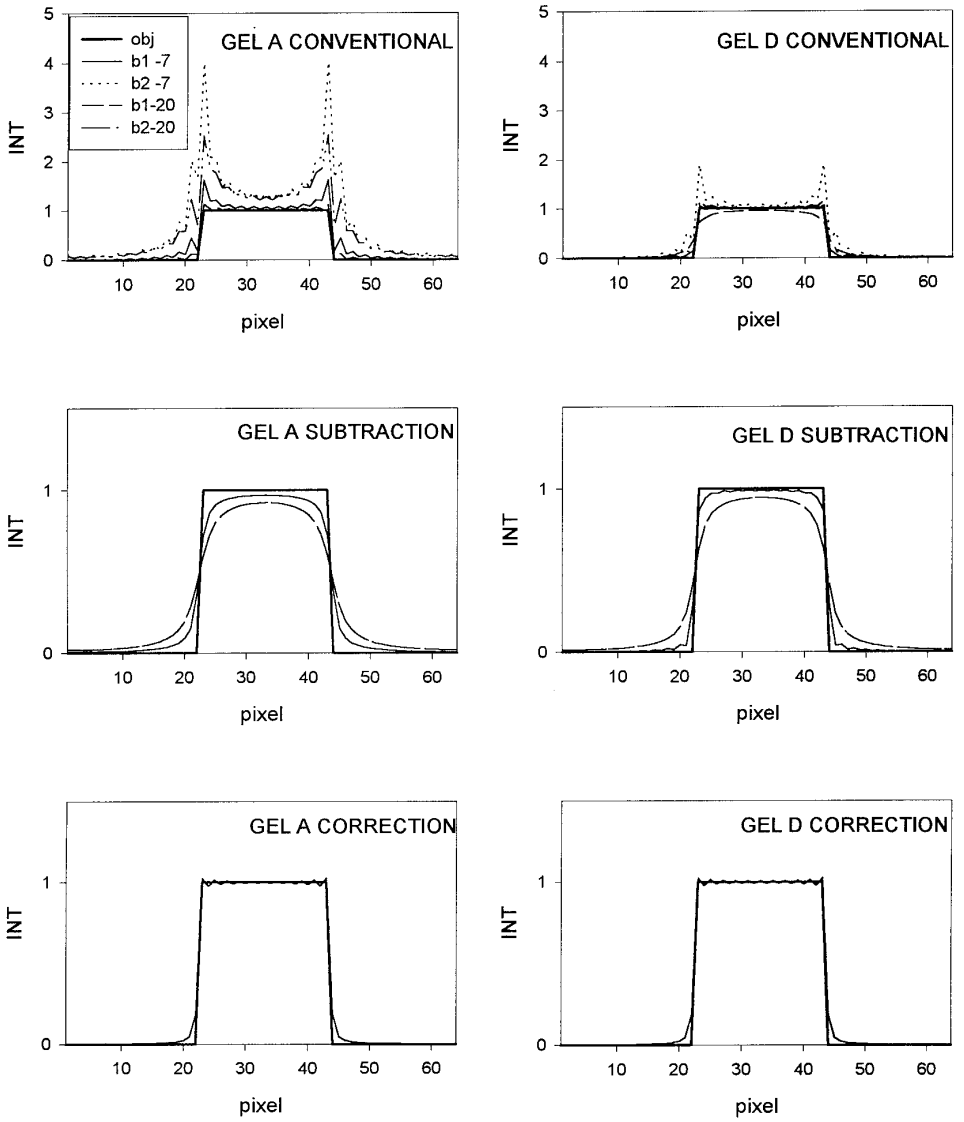

FIG. 4. Calculated image profiles are shown for $b_1 = 10$ and $b_2 = 72{,}537$ s/cm^2, and for flip angles of $\alpha = 7°$ and $\alpha = 20°$. Normalized signal curves were used in the calculation of these image profiles and could therefore by compared with the original object profile (''obj''). The left column and right column represent the calculated profiles for gel A and gel D, respectively. Top row: Conventional sequence; middle row: subtraction sequence; bottom row: correction sequence.

weighted images acquired with $b = 10$ and 72,537 s/cm^2 are shown for $\alpha = 7°$ only (columns 1 and 2, respectively), while the calculated diffusion maps are shown in column 3 for $\alpha = 7°$ and column 4 for $\alpha = 20°$. The images show an edge-enhancement artifact for the conventional sequence (top row), which is amplified for large b values. This finding is consistent with the high-pass characteristic of the normalized signal curves. The artifact is characterized by a ''sawtooth'' pattern which is reflected as a secondary rim along the phase-encoding direction on the diffusion-weighted images. The rims are still present in the calculated maps. Similarly, a smoothing effect is noticeable for the subtraction sequence (second row) corresponding to the low-pass filter characteristic of the signal curves, as shown in Fig. 2 (middle). As mentioned in the previous section, this effect is now identical for each b value and will consistently be propagated in the calculation of the diffusion map where it will produce a broadening of the calculated diffusion map. This is most visible for the diffusion map obtained with $\alpha = 20°$.

The third row in Figs. 4 and 5 exhibits the profiles and images for the correction sequence. The edge artifacts are absent, which agrees with the flat signal curves of Fig. 2 (bottom). However, a smearing effect is noticed in the phase-encoding direction, e.g., the DC spot, which can be

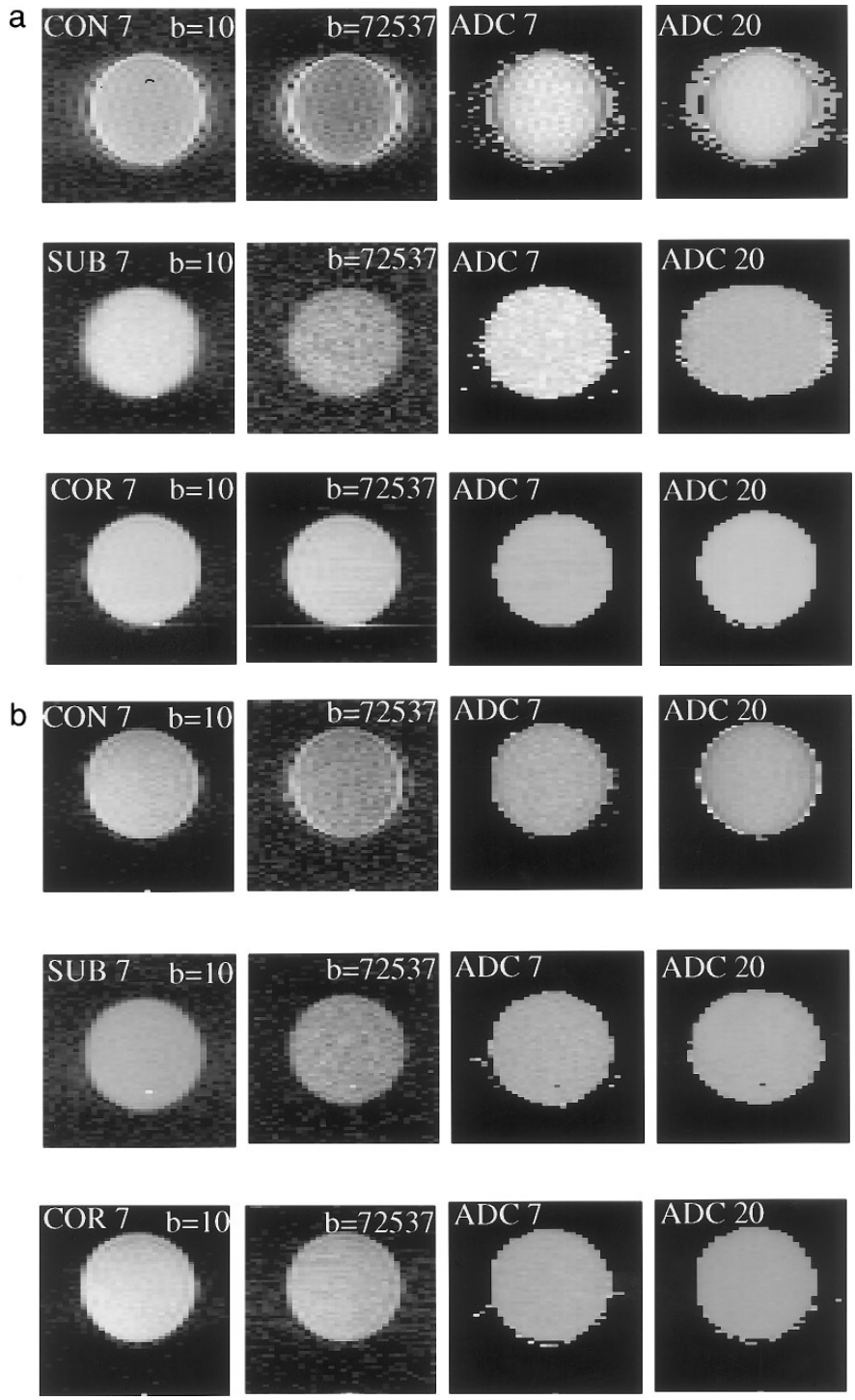

FIG. 5. Diffusion-weighted images associated with the simulated image profiles of Fig. 4. Images are presented for the conventional sequence (top row), the subtraction sequence (middle row), and the correction sequence (bottom row). (a) Images for gel A (T_1 = 217 ms) are shown for $\alpha = 7°$ with $b = 10$ s/cm^2 and $b = 72{,}537$ s/cm^2 in the first and second column, respectively. Columns 3 and 4 are calculated diffusion maps which were obtained from a series of five to seven diffusion-weighted images acquired with $\alpha = 7°$ (column 3) and $\alpha = 20°$ (column 4). The images were scaled individually for reasons of display. (b) Images for gel D (T_1 = 1.102 s): The typical artifacts on the images are still visible, although less pronounced due to the larger T_1 value.

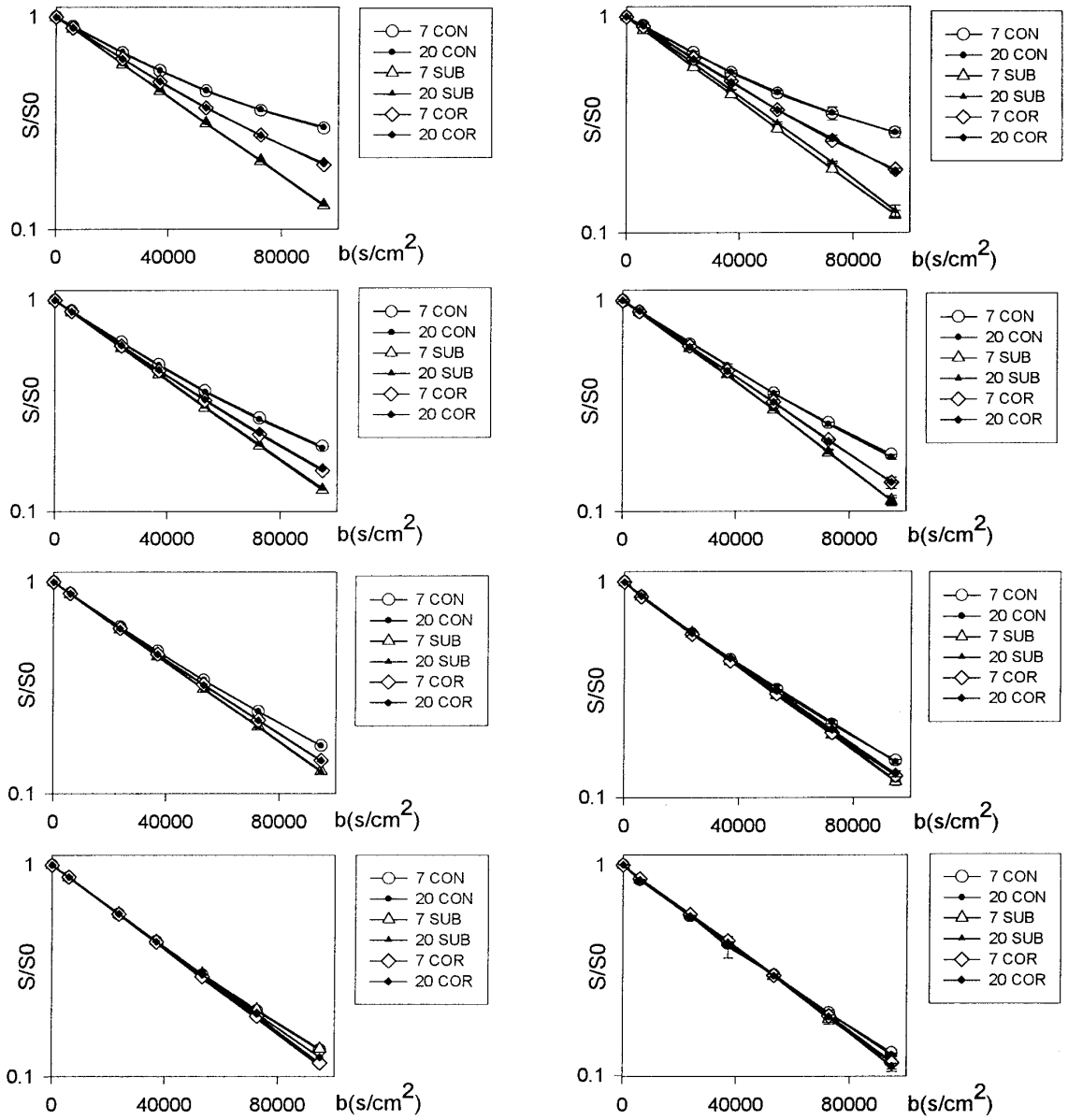

FIG. 6. Semilogarithmic calibration plots are shown for the conventional sequence (''CON''), the subtraction sequence (''SUB''), and the correction sequence (''COR''). Computer simulations (including slice effects, left column) as measurements (right column) were conducted for nominal flip angles of 7° (open symbols) and 20° (filled symbols). The experimental data points are displayed as means ± SD ($n = 6$) and are interconnected with lines. In most cases the error bars were smaller than the symbols. The plots were normalized to the first data point for reasons of display only. The results are presented for all samples: gel A (top row), gel B (second row), gel C (third row), and gel D (bottom row).

explained by the fact that the correction consists of multiplying the full echo signal with the function $1/w(n)$ (see Eq. [10]). Therefore, a constant signal will in turn be weighted by $1/w(n)$ and the smearing will be proportional to the extent to which the data must be corrected. Similarly, the noise in different *k*-space lines will be unequally weighted depending on the function $1/w(n)$. The images for the sample with the largest T_1 value are shown in Fig. 5b. The artifacts specific for each sequence are still present but are less severe than those for the first sample. This is because T_1-related terms become less important for increasing T_1 values: in the expressions they appear as $\exp(-\mathrm{TR}/T_1)$ and $\exp(-\tau/T_1)$ which become 1 for the case $T_1 = \infty$.

For the subtraction sequence, the term responsible for the filter effect is described in Eq. [14] by $[E_1\cos(\alpha)]^{n-1}$ and is clearly independent of the *b* factor. This suggests that a compensation can be envisaged by using a variable-flip-angle series which is common to all *b* values.

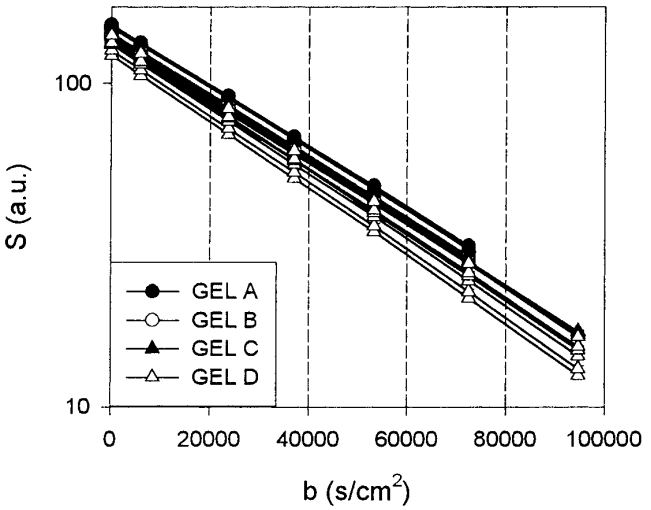

FIG. 7. Calibration plots for the set of spectroscopic reference measurements. The data points are presented as means ± SD (n = 4 to 6) with interconnecting lines. The linear relationship is obvious and a linear regression of the data resulted in correlation coefficients r^2 of 1.000 in most cases, and 0.9988 at worst, for some cases with gel D.

Accuracy Considerations

Semilogarithmic attenuation plots are shown in Fig. 6 for all the experiments. It is clear that a substantial deviation from linearity exists for the conventional sequence and for the correction sequence. This deviation can be ascribed to the diffusion-independent terms $B(n)$ and $F(n)$ in Eq. [6] and Eq. [13], respectively. Although these values are zero for the most important excitation step, i.e., $B(n = 1) = 0$ and $F(n = 1) = 0$, the results show that subsequent steps do have an influence on the main intensity in the images. The term $B(n)$ has two contributions coming from the longitudinal relaxation during the time τ and during the imaging period TR, while only the contribution from the delay τ is contained in $F(n)$. Correcting for the relaxation during the period TR, as the correction sequence does, is clearly not sufficient to fully eliminate the error. The longitudinal relaxation during the small delay τ (τ = 4.882 ms, $\tau/T_1 = 0.02$ for the smallest T_1) is large enough to generate systematic errors. This may cause a problem when a larger delay would have to be used for gradient preparation in order to reduce eddy-current effects (*14*). Finally, when considering the plots in Fig. 6, it can be understood why deviations were not observed in previous work: Here either a low range of b factors was used [20,000 s/cm^2 (*11*)] on samples with various T_1 values or b factors up to 59,000 s/cm^2 were applied on samples with high T_1 values (pure water) (*12*).

The good agreement between theoretical and experimental findings and the fact that the spectroscopic reference measurements show a linear plot (Fig. 7) indicates that the deviations are not due to other physical effects such as the presence of local gradients or the existence of multiple diffusion compartments. Cross-term effects between gradient pulses are also to be excluded since they would have pro-

TABLE 2
Results (in 10^{-5} cm^2/s) of Computer Simulations from TurboFLASH Including Slice Effects

Technique:	Conventional		Subtraction		Correction	
α:	7°	20°	7°	20°	7°	20°
Gel A						
Input	2.153	2.145	2.153	2.145	2.153	2.145
(1)	1.41 ± 0.07	1.39 ± 0.07	2.157 ± 0.003	2.149 ± 0.003	1.80 ± 0.04	1.79 ± 0.04
(2)	2.16 ± 0.01	2.15 ± 0.01			2.15 ± 0.02	2.15 ± 0.04
Gel B						
Input	2.183	2.164	2.183	2.164	2.183	2.164
(1)	1.82 ± 0.05	1.80 ± 0.05	2.187 ± 0.003	2.168 ± 0.003	2.03 ± 0.02	2.01 ± 0.02
(2)	2.19 ± 0.01	2.17 ± 0.01			2.18 ± 0.01	2.16 ± 0.01
Gel C						
Input	2.167	2.175	2.167	2.175	2.167	2.175
(1)	1.97 ± 0.03	1.97 ± 0.03	2.171 ± 0.003	2.179 ± 0.003	2.08 ± 0.01	2.09 ± 0.01
(2)	2.18 ± 0.01	2.18 ± 0.01			2.17 ± 0.01	2.18 ± 0.01
Gel D						
Input	2.381	2.368	2.308	2.273	2.308	2.273
(1)	2.22 ± 0.03	2.20 ± 0.03	2.312 ± 0.003	2.279 ± 0.003	2.25 ± 0.01	2.21 ± 0.01
(2)	2.38 ± 0.01	2.37 ± 0.01			2.31 ± 0.01	2.27 ± 0.01

Note. Results (means ± SE) from nonlinear-least-square fit to (1) $A \exp(-bD)$ and (2) $A \exp(-bD) + B$. Input: Diffusion coefficients taken as input value for the simulation.

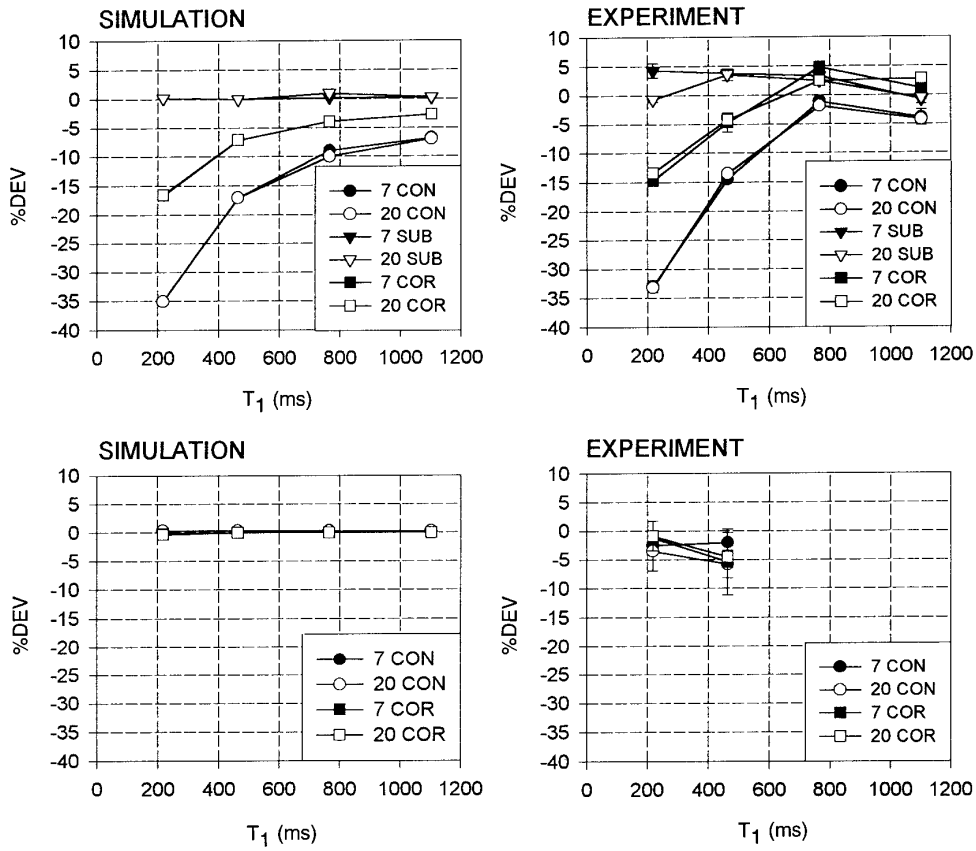

FIG. 8. Plot of the %DEV = $[(D_{im} - D_{ref})/D_{ref}] \times 100$ versus T_1 for all samples, where D_{im} stands for the diffusion coefficient derived from simulated image profiles (left column) or from acquired images (right column). D_{ref} is the diffusion coefficient taken as the input parameter for the simulations or is the diffusion coefficient determined from the spectroscopic measurements. The top row shows the percentage deviation from the reference values when the expression $A \exp(-bD)$ is used for deducing the coefficient D, whereas the expression $A \exp(-bD) + B$ is used for the bottom row.

duced identical deviations for all samples (the samples have almost identical diffusion coefficients). When pooling the totality of the spectroscopic results ($n = 24$) per sample, the diffusion coefficients amount to $2.151 \pm 0.009 \times 10^{-5}$ cm^2/s for gel A, $2.178 \pm 0.008 \times 10^{-5}$ cm^2/s for gel B, $2.160 \pm 0.009 \times 10^{-5}$ cm^2/s for gel C, and $2.305 \pm 0.057 \times 10^{-5}$ cm^2/s for gel D. The temperature registered on the average in the magnet bore was 22.4°C for which a diffusion coefficient of 2.2×10^{-5} cm^2/s is found for water (*1*). The small standard deviations indicate that ambient conditions were stable during the measurement sessions, except for gel D where a systematic decrease was noted going from 2.38 to 2.23×10^{-5} cm^2/s. With a temperature dependence of 2.4%/°C (water), this corresponded to a temperature change of 2.6°C.

The results are summarized in Table 2 for the simulations and in Table 3 for the experiments. From Table 2, one can see that the measured diffusion coefficient is underestimated by the conventional and the correction sequence, even for the sample with the largest T_1 value. This is reflected as slight deviations from linearity on the corresponding curves in Fig. 6. The results in Table 2 confirm that the accuracy of the estimation of the diffusion coefficient may be improved when fitting the data to $A \exp(-bD) + B$ since this expression is better suited to describe the physical model for these sequences (see Eqs. [6] and [13]). The same conclusion is valid for the experimental data presented in Table 3, where the accuracy could again be improved by including an additional constant term. However, when fitting the data, the error on the fitted parameter B became very large in some cases. In Table 3 only the cases for which a t test on this parameter gave values of $t > 10$ ($P < 0.01$) were included. In other words, only those cases were retained for which the parameter B led to an improved prediction of the dependent variable D.

The systematic error in the calibration measurements was quantified by calculating a percentage deviation, defined as %DEV = $[(D_{im} - D_{ref})/D_{ref}] \times 100$. The diffusion coefficient D_{im}, derived from simulated image profiles or from imaging experiments, is compared to D_{ref} which is used as

TABLE 3
Experimental Results (in 10^{-5} cm^2/s) from Samples Using TurboFLASH Diffusion-Weighted Imaging

Technique:	Conventional		Subtraction		Correction	
α:	7°	20°	7°	20°	7°	20°
Gel A						
Spect.	2.156 ± 0.006	2.148 ± 0.004	2.143 ± 0.007	2.148 ± 0.008	2.153 ± 0.005	2.145 ± 0.005
Im$^{(1)}$	1.45 ± 0.02	1.44 ± 0.01	2.24 ± 0.03	2.14 ± 0.01	1.84 ± 0.02	1.86 ± 0.02
Im$^{(2)}$	2.13 ± 0.06	2.10 ± 0.08				
Gel B						
Spect.	2.190 ± 0.005	2.177 ± 0.001	2.152 ± 0.016	2.172 ± 0.013	2.188 ± 0.018	2.192 ± 0.007
Im$^{(1)}$	1.87 ± 0.02	1.90 ± 0.04	2.23 ± 0.01	2.25 ± 0.02	2.09 ± 0.04	2.10 ± 0.02
Im$^{(2)}$	2.18 ± 0.08	2.18 ± 0.06				
Gel C						
Spect.	2.170 ± 0.007	2.165 ± 0.016	2.192 ± 0.007	2.187 ± 0.009	2.154 ± 0.005	2.158 ± 0.004
Im$^{(1)}$	2.15 ± 0.01	2.13 ± 0.01	2.27 ± 0.02	2.24 ± 0.01	2.26 ± 0.02	2.21 ± 0.02
Gel D						
Spect.	2.381 ± 0.006	2.368 ± 0.008	2.308 ± 0.014	2.273 ± 0.010	2.251 ± 0.007	2.232 ± 0.010
Im$^{(1)}$	2.29 ± 0.03	2.27 ± 0.02	2.29 ± 0.02	2.26 ± 0.01	2.27 ± 0.02	2.32 ± 0.02

Note: Im$^{(1),(2)}$: Results (means ± SD; $n = 6$) from turboFLASH images fitted to $^{(1)}A \exp(-bD)$ and $^{(2)}A \exp(-bD) + B$. Spect: Results (means ± SD, $n = 4-6$) from spectroscopic diffusion measurements fitted to $A \exp(-bD)$.

input for the simulations or is extracted from the spectroscopic reference measurements. In Fig. 8 the %DEV has been plotted against T_1 for the complete set of simulations (left) and measurements (right). Although differences are found for some points between simulation and experiment, the general appearance is very similar. The figures show that, when using the conventional sequence, the deviations amounted to −33% for the sample with the smallest T_1. The error decreases for larger T_1 values but can still add up to 10% for the conventional sequence and 5% for the correction sequence when $T_1 \approx 800$ ms. The simulations show that even for $T_1 = 1.1$ s, the deviation is not strictly zero. This has its importance in the light of using turboFLASH to acquire diffusion data at low magnetic fields. For instance, at 1.5 T, T_1 values around 1000 and 710 ms are found for gray and white matter, respectively (*27*). As already shown in Tables 2 and 3, the errors are significantly reduced ($P < 0.05$) when the second expression is used to fit the data for the conventional and the correction sequence (Fig. 8, bottom left and right). The error is eliminated when using the subtraction sequence.

Neglecting slice effects in the simulations did not produce major changes in the results. An explanation can be found in the observation (based on simulation and measurement) that distortions of the slice shape occur only from about the 10th excitation step onward, when most intense lines have already been acquired. Therefore no appreciable influence on the mean intensity of the images is expected. Simulations performed for smaller flip angles, down to 4°, did not improve the results either. This is understandable when we consider how the relative contributions of the diffusion-independent term $B(n)$ and the diffusion-dependent term $A(n)$ are changing with the excitation step n for different flip angles. For a range going from 4° to 20°, the change of the ratio $B(n)/[A(n)\exp(-bD)]$ with n coincides for the first six to eight excitation steps. This indicates that their relative contribution is independent of the flip angle during the first excitation steps. Again, for centric phase encoding most of the signal is acquired during these steps, and no major influence of the flip angle on the calibration results is expected. This is also apparent in Fig. 6 where the plots for 7° and 20° coincide. Another consequence of the centric phase-

TABLE 4
Signal-to-Noise Ratios Measured on Rat Brain Images (Cortex/Background)

Technique:	Conventional		Subtraction		Correction			
α:	7°	20°	7°	20°	7°	20°	Spin echo	
$b = 12$	12	37	16	36	17	23	$b = 2262$	24
$b = 97306$	6	19	8	17	12	18	$b = 83524$	15

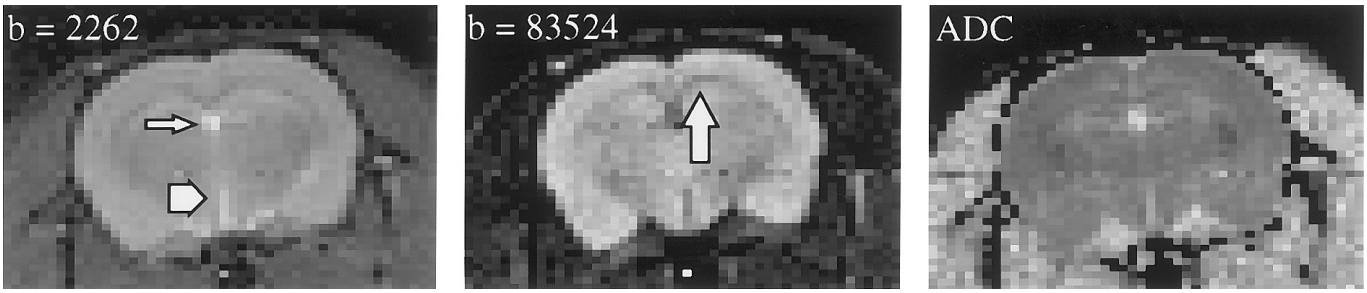

FIG. 9. ECG-triggered navigator-corrected diffusion-weighted spin-echo images and associated calculated ADC map (right) of the rat brain. Sequence parameters: $TR_{min}/TE = 6000/48$ ms, $\Delta = 26$ ms, $\delta = 13.5$ ms, 3×4.5 cm^2 FOV, NEX = 1, 64×128 matrix, and 2.2 mm slice. The calculated map was obtained from eight diffusion-weighted images with *b* factors taken within a range of 2262 to 195,688 s/cm^2. Diffusion gradients were applied along the slice-select direction. Regions with high ADC values are hypointense on the diffusion-weighted images, whereas they are hyperintense in the calculated ADC maps. In the left image, the dorsal part (white arrow) and the ventral part (white arrowhead) of the third ventricle are visible, while the corpus callosum is denoted in the middle image (white arrow).

encoding scheme is that the same errors may be expected for small and large matrix sizes since they share the first excitation steps.

Finally, the results did improve when the simulations were performed for smaller repetition times TR. For instance, for the conventional sequence, a simulation performed with TR = 3.5 ms reduced the deviation from about −33 to −21% for T_1 = 200 ms, −10 to −7% for T_1 = 800 ms and −5 to −4% for T_1 = 1.1 s. The effort to bring down the repetition time to 3.5 ms is beneficial, but insufficient for smaller T_1 values.

In Vivo

The three sequences were also applied to obtain diffusion-weighted images of the rat brain *in vivo*. Typical values for

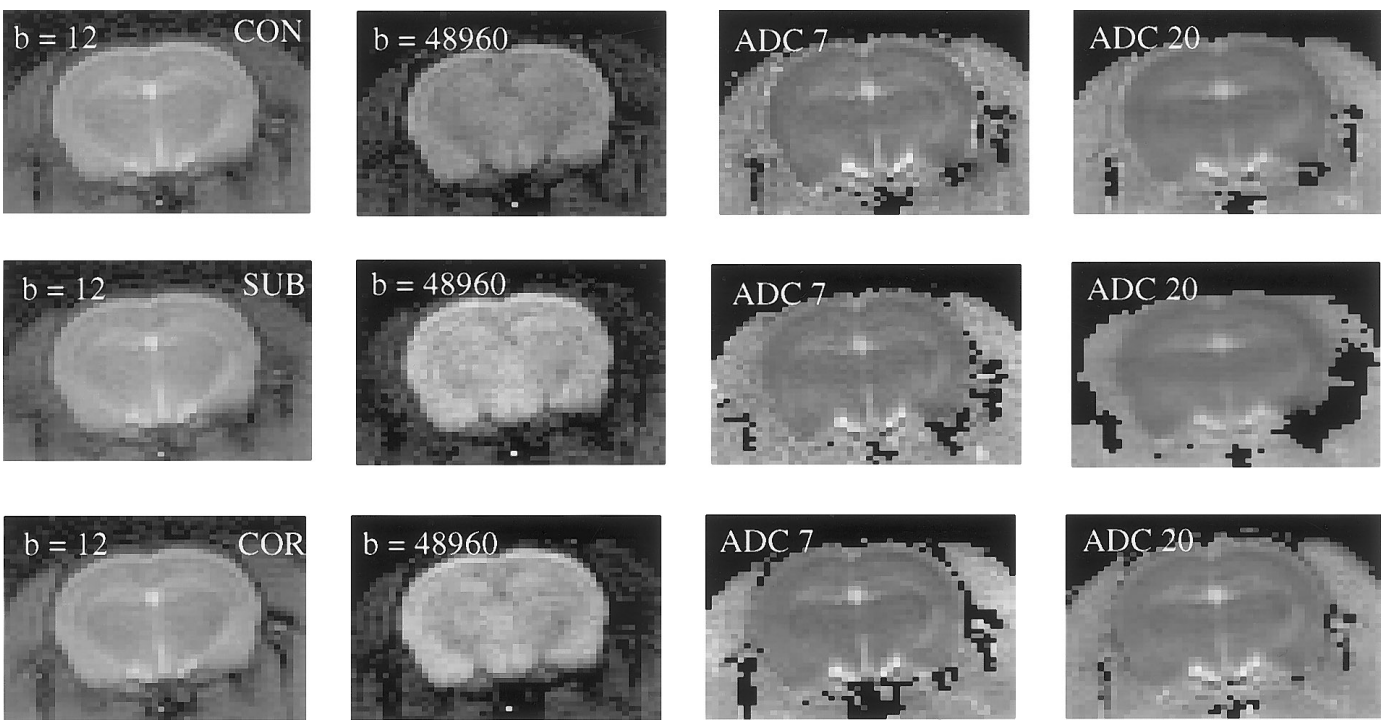

FIG. 10. ECG-triggered diffusion-weighted turboFLASH images and calculated ADC maps of the rat brain. The images are scaled individually to provide a proper display. The images are acquired with a slice thickness of 2.2 mm, 3×4.5 cm^2 FOV, 64×128 matrix, NEX = 8, $TE_p = 37$ ms, $\delta = 13.5$ ms, and $\Delta = 17.5$ ms. Images in the top row were obtained with the conventional sequence, the second row shows the images for the subtraction sequence, and the third row shows the images for the correction sequence. The calculated maps were obtained from six to seven diffusion-weighted images depending on the signal-to-noise ratios in the most heavily diffusion-weighted image.

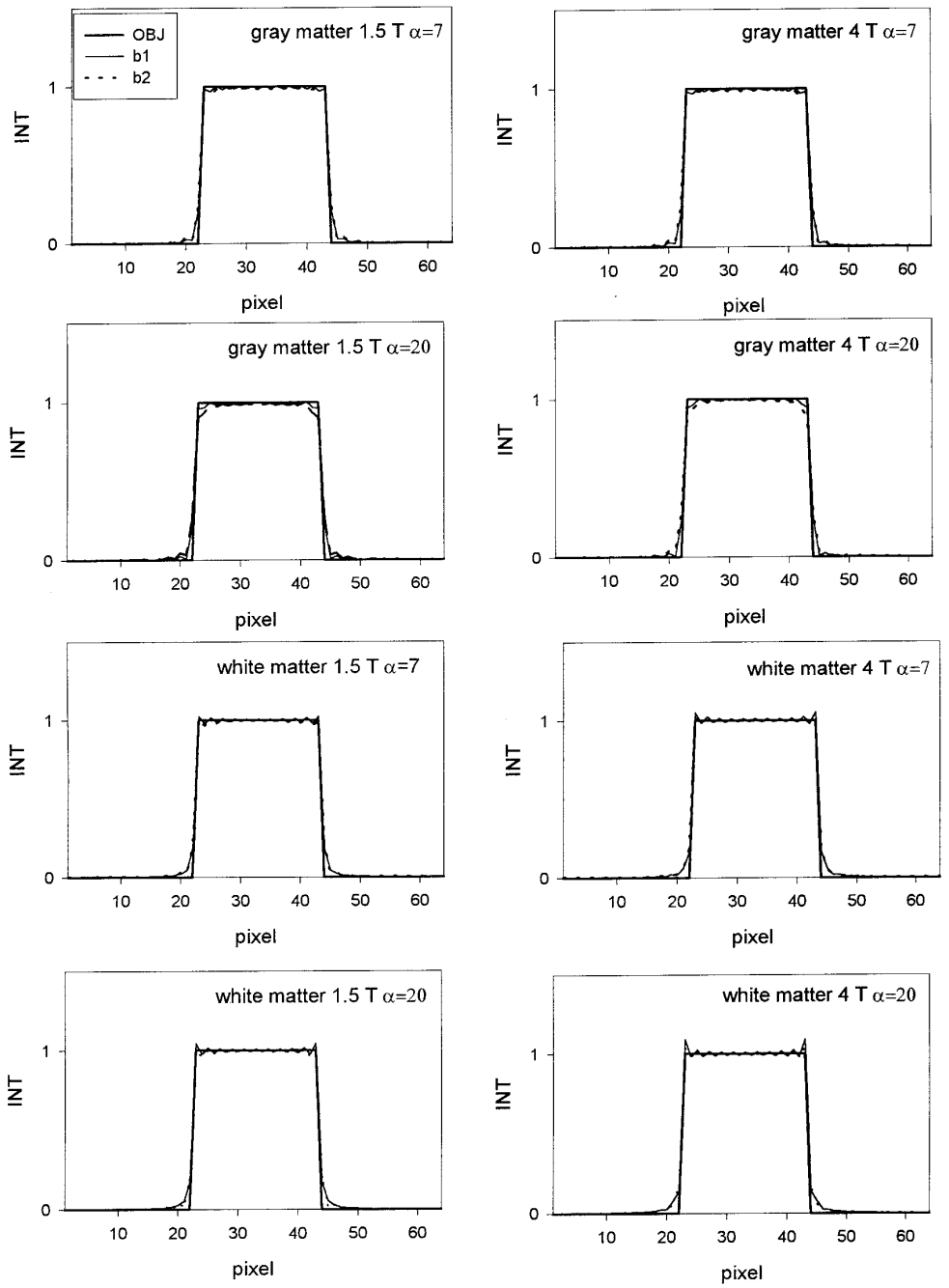

FIG. 11. Calculated image profiles for an object with properties of gray matter (GM) and white matter (WM). Simulations were performed for field strengths of 4 T‖1.5 T, respectively, with T_1/T_2 (GM) = 1.724/0.063s‖1.000/0.085, T_1/T_2 (WM) = 1.043/0.050 s‖0.710/0.075, ADC (GM and WM) = 0.70 10^{-5} cm^2/s, T_1/T_2 (muscle) = 1.830/0.026 s‖0.980/0.031, and ADC (muscle) = 1.5 10^{-5} cm^2/s. The profiles are calculated for the correction sequence where the correction is performed with a function corresponding to the mean values for GM, WM, and muscle. (b_1 = 10 s/cm^2, b_2 = 72,537 s/cm^2).

the SNR (cortex/background) are given in Table 4. The difference of the SNR for the correction sequence with respect to the other two sequences can be explained by the unequal weighting of the noise in each k-space line. For instance, a high-pass k-space filter w(n) may be expected for the smallest flip angle and large diffusion weighting. The correction 1/w(n) will therefore consist of a low-pass filter which will reduce the noise for higher excitation steps.

Apparent-diffusion-coefficient (ADC) maps were derived and compared with the calculated maps obtained from navi-

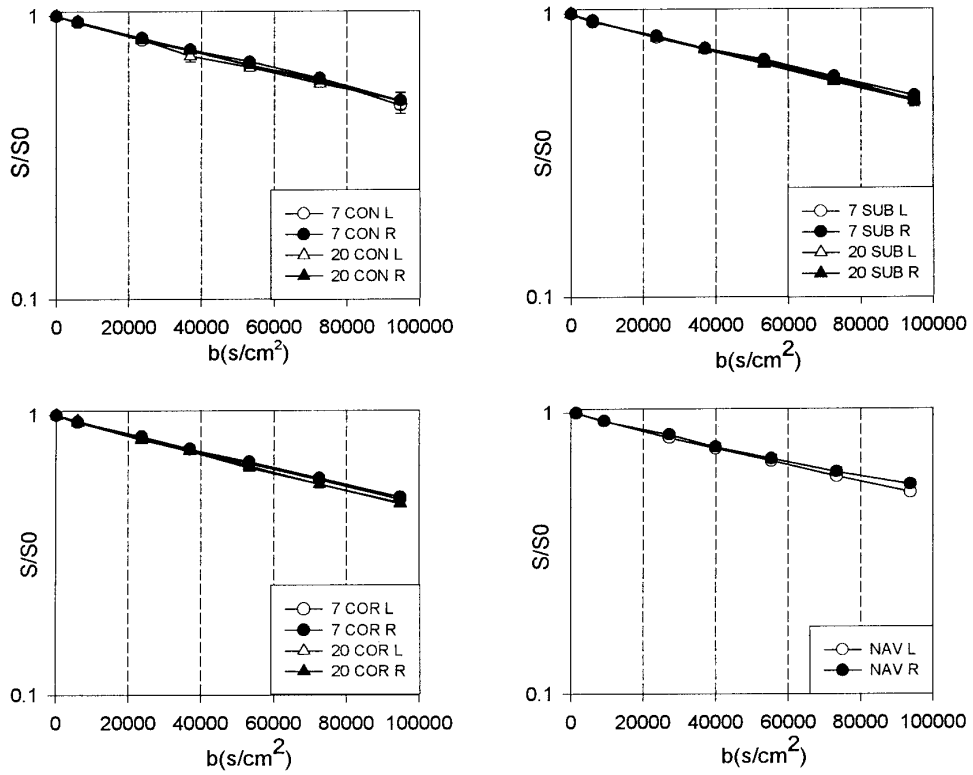

FIG. 12. Semilogarithmic plots for rat brain. Plots are normalized to the first data point and are shown for the spin-echo sequence (bottom right) and for the turboFLASH sequences (α = 7° and 20°): conventional sequence (top left), subtraction sequence (top right), and correction sequence (bottom left). Data were taken from a ROI in the left (L) and right (R) hemisphere of the neocortex.

gator-corrected diffusion-weighted spin-echo images (Fig. 9). Visual comparison of images is of course a subjective matter, but the turboFLASH images in Fig. 10 show that the predicted filter effects are discernible. For instance, a smoothing effect is most apparent in the diffusion maps calculated for the largest flip angle (column 4). In fact, on the basis of the phantom experiments, no image artifacts were expected for the correction sequence. Several causes could be at the origin of the disagreement with the expected result. First, to attain a perfect compensation, the imaging data set and the correction data set [represented earlier as the function $w(n)$] must be submitted to identical filter properties. A departure from this case is possible since both data sets were acquired sequentially instead of interleaved with a time interval of about fifteen minutes. Second, it has been recently shown (*26*) that the phase-encoding order has an influence on the time course of the signal. Therefore, a difference may be expected between the time course of $w(n)$ (acquired without phase-encoding gradient) and the imaging data (acquired with phase-encoding gradient). While this effect cannot be excluded, the effect would also have appeared in the phantom experiments were none of such large smoothing artifact was seen in these experiments. Third, the individual structures, e.g., gray matter, may have been corrected with a nonadapted function, common to the totality of the structures (i.e., muscle, white matter, gray matter, CSF) in the image. To illustrate this last effect, image profiles were calculated for a one-dimensional object with properties of gray matter (GM) and white matter (WM), but corrected with a function corresponding to the mean values of GM, WM, and muscle. Only these structures were chosen because they form the largest fraction of the tissue in the slice. Values for T_1 and T_2 were taken for main fields of 4 and 1.5 T (*27–29*). The results in Fig. 11 show that, even for the correction sequence, small edge artifacts may be expected in the form of an edge enhancement for white matter and a smoothing effect for gray matter. The artifacts are expected to be more pronounced for larger b values and larger flip angles but are not very sensitive to the main field.

Semilogarithmic plots of the data taken in a ROI in the neocortex are presented in Fig. 12. The plots show no major deviation from a linear relationship for the chosen range of b factors, which is consistent with Fig. 8, considering that T_1 for rat cortex has been found to be around 0.9 to 1.7 s at 4.7 T (*30, 31*). The plots for α = 7° and 20° and for ROI taken in the left and right hemisphere are nearly overlapping. The former confirms the results of the phantom experiments while the latter indicates the absence of major asymmetries

TABLE 5
Experimental Results (in 10^{-5} cm^2/s) from Rat Brain Using TurboFLASH and Spin-Echo Diffusion-Weighted Imaging

Technique:	Conventional		Subtraction		Correction		
α:	7°	20°	7°	20°	7°	20°	Spin echo
Cortex	0.66 ± 0.03 (0.59–0.70)	0.69 ± 0.03 (0.61–0.73)	0.63 ± 0.03 (0.62–0.70)	0.69 ± 0.03 (0.63–0.74)	0.67 ± 0.03 (0.62–0.72)	0.73 ± 0.05 (0.67–0.79)	0.63 ± 0.03 (0.58–0.66)

Note. Results from ROI data taken in diffusion maps of the rat brain (means ± SD, $n = 11$ for turboFLASH and $n = 8$ for spin echo). The ADC were obtained by nonlinear-least-squares fit to $A \exp(-bD)$. Literature: $0.726 \pm 0.022 \times 10^{-5}$ cm^2/s (*5*); $0.630 \pm 0.075 \times 10^{-5}$ cm^2/s (*31*); $0.615 \pm 0.079 \times 10^{-5}$ cm^2/s (*32*).

in the imaging setup. The results taken from ROI in the ADC maps of Figs. 9 and 10, pooled over the two hemispheres, are summarized in Table 5. No significant difference ($P < 0.01$) was found between the results obtained from the spin-echo sequence and the turboFLASH sequences with $\alpha = 7°$. A significant difference ($P < 0.01$) with respect to the spin-echo case and the $\alpha = 7°$ case did exist for $\alpha = 20°$. We ascribe this to the increased blurring combining tissue-to-tissue overlap of regions with different diffusion coefficients present within these ADC maps. Despite these differences, the results do agree with the range of values reported by others on rat brain (Table 4).

CONCLUSION

The experiments on phantoms have shown that a systematic error is induced by longitudinal relaxation in diffusion measurements performed with the conventional centric phase-encoded turboFLASH sequence. The errors are particularly large for smaller T_1 values, e.g., in a range from 200 to 800 ms, which includes T_1 values of brain tissues at low fields. At first sight, the deviation could be mistakenly interpreted as a multidiffusion compartment phenomenon. Correction for the longitudinal relaxation effects during the imaging time is not sufficient, since longitudinal relaxation during the spoiling period τ may still induce significant errors, thereby limiting the use of this delay for purposes of gradient preparation. The influence of T_1 effects is eliminated by the subtraction sequence, which gives the most accurate results for a large range of T_1 values. The application of this sequence is accompanied with image artifacts which, as we anticipate, could be reduced by using a variable-flip-angle series.

We restricted our *in vivo* study to a representative slice position in rat brain which was chosen according to a position which will be used in a localized stroke model (*33*). Our conclusions are therefore only relevant for this case. The *in vivo* example demonstrates that for conditions of rat brain at a field of 4.7 T, artifacts in the calculated ADC maps are more pronounced for larger flip angles, thereby limiting the use of large flip angles for signal-to-noise improvement. The artifacts are reflected by a loss of edge definition which tends to obscure the details in the images. These findings may be important in the detection of small stroke lesions in animals, since an accurate assessment of the lesion area, and changes thereof, could be impaired when using these sequences. The presence of artifacts is, however, less crucial for small flip angles ($\alpha = 7°$ in our case). Furthermore, for small flip angles, no difference was found for the estimated ADC values between the turboFLASH sequences and the spin-echo sequence. In general, the ADC values were in good agreement with literature data. As a consequence, in the range of b values used, no overwhelming preference for any of the sequences could be made based on our *in vivo* results. The conventional sequence is therefore to be preferred because the image data can be acquired in half the time required for the other two sequences.

APPENDIX: NOMENCLATURE

b	b factor due to diffusion and imaging gradients
b_0	b factor due to imaging gradients
D	Diffusion coefficient
DWI	Diffusion-weighted imaging
E_1	Symbol for $\exp(-\mathrm{TR}/T_1)$
E_2	Symbol for $\exp(-\mathrm{TE}/T_2)$
ECG	Electrocardiogram
FLASH	Fast low-angle shot
f_y	Spatial frequency in the y direction
G_y	Phase-encoding gradient amplitude
$I(y_j)$	Image of one-dimensional object
$M_t(n)$	Transverse magnetization after nth RF pulse
$M_{t,\mathrm{im}}(n)$	Transverse magnetization after nth RF pulse in image data
$M_t'(n)$	Transverse magnetization after nth RF pulse, acquired without phase encoding
$M_{t,\mathrm{corr}}(n)$	Transverse magnetization after nth RF pulse for corrected image data
$M_z(n, -)$	Longitudinal magnetization before nth RF pulse

$M_z(n, +)$	Longitudinal magnetization after nth RF pulse
M_0	Equilibrium magnetization
N	Number of samples in the phase-encoding direction
n	Excitation step
NEX	Number of excitations
$s(f_y)$	Fourier transform of one-dimensional object
$s'(f_y)$	Fourier transform of one-dimensional object weighted with k-space filter
T	Duration of phase-encoding gradient
TR	Repetition time in FLASH imaging sequence
TE	Echo time in FLASH imaging sequence
TE_p	Time between two 90° RF pulses in preparation period
$w(n)$	Function which is used to correct the image data in the correction sequence
α	Flip angle in FLASH imaging sequence
δ	Duration of diffusion gradient pulses
ϵ	Rise and set time of diffusion gradient pulse
Δ	Duration between leading edges of diffusion gradients
ρ	Spin density
τ	Time delay between preparation period and FLASH imaging sequence

ACKNOWLEDGMENTS

This work was supported by the Belgian Programme on Interuniversity Attraction Poles initiated by the Belgian State–Prime Minister's Office–Science Policy programming. The authors thank Dr. V. Jellus from the SAS, Bratislava, Slovakia, for writing software for data transfer and E. Broothaers for his photographic work.

REFERENCES

1. D. Le Bihan and R. Turner, ''Magnetic Resonance Imaging'' (D. D. Stark and W. G. Bradley, Eds.), Vol. 1, Chap. 13, Mosby Year Book, St. Louis, 1992.
2. M. E. Moseley, Y. Cohen, J. Mintorovitch, L. Chileuitt, H. Shimizu, J. Kucharczyk, M. F. Wendland, and P. R. Weinstein, *Magn. Reson. Med.* **14,** 330–346 (1990).
3. S. Warach, D. Chien, W. Li, and R. R. Edelman, *Neurology* **42,** 1717–1723 (1992).
4. K. Minematsu, L. Li, M. Fisher, C. H. Sotak, M. A. Davis, and M. S. Fiandaca, *Neurology* **42,** 235–240 (1992).
5. M. Hoehn-Berlage, D. G. Norris, K. Kohno, K. Kohno, G. Mies, D. Leibfritz, and K-A. Hossmann, *J. Cereb. Blood Flow Metab.* **15,** 1002–1011 (1995).
6. B. J. Dardzinski, C. H. Sotak, M. Fisher, Y. Hasegawa, L. Li, and K. Minematsu, *Magn. Reson. Med.* **30,** 318–325 (1993).
7. R. Turner and D. LeBihan, *J. Magn. Reson.* **86,** 445–452 (1990).
8. A. Haase, *Magn. Reson. Med.* **13,** 77–89 (1990).
9. E. D. Becker, J. A. Ferretti, and T. C. Farrar, *J. Am. Chem. Soc.* **91,** 7784–7785 (1969).
10. M. Deimling, E. Müller, G. Laub, M. Recht, and R. Kroeker, *J. Magn. Reson. Imaging* **1,** 202 (1991).
11. J. E. Kirsch, Abstracts of the Society of Magnetic Resonance in Medicine, 10th Annual Meeting, p. 774, 1991.
12. H. Lee and R. R. Price, *J. Magn. Reson. Imaging* **4,** 837–842 (1994).
13. J. Coremans, M. Spanoghe, J. Sterckx, R. Luypaert, H. Eisendrath, and M. Osteaux, Abstracts of the International Society of Magnetic Resonance, 4th Scientific Meeting, p. 1340, 1996.
14. J. P. Muggler III, T. A. Spraggins, and J. R. Brookman, *J. Magn. Reson. Imaging* **1,** 731–737 (1991).
15. T. Yamazaki, T. Miyazaki, H. Toyoshima, and T. Maki, Abstracts of the Society of Magnetic Resonance in Medicine, 10th Annual Meeting, p. 852, 1991.
16. Y. De Deene, J. De Poorter, C. De Wagter, and E. Achten, Abstracts of the Society of Magnetic Resonance, 2nd Annual Meeting, p. 1066, 1994.
17. W. Hänicke, K. D. Merboldt, D. Chien, M. L. Gyngell, H. Bruhn, and J. Frahm, *Med. Phys.* **17,** 1004–1010 (1990).
18. J. Mattiello, P. J. Basser, and D. LeBihan, *J. Magn. Reson. A* **108,** 131–141 (1994).
19. H. Z. Wang and S. J. Riederer, *Magn. Reson. Med.* **15,** 175–191 (1990).
20. A. P. Crawley, M. L. Wood, and R. M. Henkelman, *Magn. Reson. Med.* **8,** 248–260 (1988).
21. R. Mathur-DeVre, R. Grimer, F. Parmentier, and J. Binet, *Magn. Reson. Med.* **2,** 176–179 (1985).
22. A. J. de Crespigny, M. P. Marks, D. R. Enzmann, and M. E. Moseley, *Magn. Reson. Med.* **33,** 720–728 (1995).
23. R. M. Henkelman, *Med. Phys.* **12,** 232–233 (1985); Erratum, *Med. Phys.* **13,** 544 (1986).
24. W. H. Press, B. P. Flannery, S. A. Teukovsky, and W. T. Vetterling, ''Numerical Recipes in C: The Art of Scientific Computing,'' Cambridge Univ. Press, Cambridge, New York, 1990.
25. A. E. Holsinger and S. J. Riederer, *Magn. Reson. Med.* **16,** 481–488 (1990).
26. F. E. Epstein, J. P. Muggler III, and J. R. Brookeman, *Magn. Reson. Med.* **35,** 237–245 (1996).
27. P. Jezzard, S. H. Duewell, and R. S. Balaban, *Radiology* **199,** 773–779 (1996).
28. S. H. Duewell, T. L. Ceckler, K. Ong, H. Wen, F. A. Jaffer, S. A. Chesnick, and R. S. Balaban, *Radiology* **196,** 551–555 (1995).
29. D. Morvan, A. Leroy-Willig, A. Malgouyres, C. A. Cuenod, P. Jehenson, and A. Syrota, *Magn. Reson. Med.* **29,** 371–377 (1993).
30. J. Detre, J. S. Leigh, D. S. Williams, and A. P. Koretzky, *Magn. Reson. Med.* **23,** 37–45 (1992).
31. M. Eis, T. Els, and M. Hoehn-Berlage, *Magn. Reson. Med.* **34,** 835–844 (1995).
32. T. Back, M. Hoehn-Berlage, K. Kohno, and K-A. Hossmann, *Stroke* **25,** 494–500 (1994).
33. B. D. Watson, W. D. Dietrich, R. Busto, M. S. Wachtel, and M. D. Ginsberg, *Ann. Neurol.* **17,** 497–504 (1985).